Applied Physics A (2018) 124:5
https://doi.org/10.1007/s00339-017-1415-2

Applied Physics A
Materials Science & Processing

Pulse energy packing effects on material transport during laser processing of $< 1|1|1 >$ silicon

Krste Pangovski[1] · Peh Siong Teh[2] · Dejiao Lin[2] · Shaiful Alam[2] · David J. Richardson[2] · William O'Neill[1]

Received: 19 June 2017 / Accepted: 16 November 2017 / Published online: 28 November 2017

Abstract
The effects of energy pulse packing on material transport during single-pulse laser processing of $< 1|1|1 >$ silicon is studied using temporarily shaped pulses with durations from 50 to 150 ns. Six regimes of material transport were identified and disambiguated through energy packing considerations over a range of pulse durations. Energy packing has been shown to shift the interaction to energetically costlier regimes without appreciable benefit in either depth, material removal or crater morphology and quality.

1 Introduction

Recent advances in fibre laser technology have furnished laser users with a large variety of parameter options. This versatility is pushing novel applications to be developed and rapidly pushed into industrial processes. However, relatively little work has been carried out to understand the material responses to complex temporal waveforms, while gaining greater insight of the key mechanisms could lead to the design of tailored waveforms that efficiently couple into the material.

Laser fabrication of high-quality, large aspect ratio holes has been driven by real-world applications ranging from via-hole drilling in the semiconductor and microelectronics industries to jet turbine blade drilling of effusion holes in the aerospace sector. Although laser-based drilling has enabled hole features which far exceed capabilities offered by mechanical counterparts, the post-process morphology is often mired by the appearance of micro-cracks or re-solidified material in or near the machined site. From this perspective it is not advantageous to remain in a melt-dominated material removal regime. The obvious solution has been to shift the interaction towards a vapour-driven process thus minimising the molten while at the same time minimising the vapour recondensate which is carried away from the crater by the vapour plume; a mechanism which is attributed to the peak pulse power. There is a wealth of literature examining laser ablation in relation to laser-induced plumes [1–6] or material ejection mechanisms [7–10]. Similarly, variation in pulse duration has been studied and applied to minimise these artefacts by reducing the interaction time. Significant advances have been made by shortening the pulse duration below the electron-phonon coupling times for a given material, thereby ablating the material before any thermal energy is transferred to the bulk substrate [11, 12].

The arrival of lasers with programmable temporal envelopes has opened up additional opportunities for novel approaches to energy-efficient material processing. Double-pulse delivery profiles in the nanosecond regime have been proposed and investigated by Forsman [13] and Wang [14] demonstrating enhanced material removal rates by tuning the delivery time of the secondary pulse. The increased penetration depth was phenomenologically attributed to a secondary, reverse travelling blast wave; a consequence of the heated cloud of ejecta vaporising [13]. Similar results were reported by Liu et al. [15] and more recently by Veiko et. al. [16]. The double-pulse approach has also been extended to femtosecond pulses by Liebig [17] showing drastic increase in ablation depth.

Similar improvements have been demonstrated using burst mode delivery, whereby a set of closely timed pulses (i.e. typically $>> 2$ pulses) are delivered to the sample [18, 19]. In their work Li et. al. [18] used 5–50 kHz bursts of front peak pulses with a gaussian temporal envelope showing a narrowing of the recast layer with no microevidence of microcracking. In

✉ Krste Pangovski
kp358@cam.ac.uk

[1] Centre for Industrial Photonics, Institute for Manufacturing, University of Cambridge, Cambridge CB3 0FS, UK

[2] Optoelectronics Research Centre, University of Southampton, Southampton SO17 1BJ, UK

Hendow's paper [19] burst mode pulsing using 10-ns-pulse bursts operating at 5 MHz also showed promising results.

Other works investigating the consequence of temporal envelope on post-process surface morphology has ubiquitously shown favourable results when applying tailored temporal envelopes for both nanosecond [20–25] and femtosecond [17, 26] pulses. More recent work on temporal profile design has also demonstrated significant improvements in surface quality using double-peak pulses with an interconnecting energy bridge [27].

These approaches have all demonstrated various levels of improvements in terms of material penetration and post-process morphology. In all cases dynamic effects such as plasmas, shockwaves and eject have been shown to have significant role in material removal and on the final outcome. In this work we use $<1|1|1>$ silicon to study the effect of optical energy packing into front peak decaying-energy tail temporal envelopes on the material transport mechanisms and post-process surface morphology.

2 Phenomenological background

Silicon is partially transparent at $\lambda = 1060$ nm with a characteristic penetration depth of $\simeq 10\,\mu$m. For molten silicon, the absorption coefficient increases by an order of magnitude (see Table 1), while the penetration depth drops dramatically with increase in temperature beyond T_m by an order of magnitude, confining the energy to a thin surface layer [27]. This type of confinement transition is unique to materials that are optically transparent to the processing wavelength and opens the possibility of tuning the temporal envelope to control the material response through tailoring the pulse shape. Depending on the ratio of the thermal and optical penetration depths, the surface temperature can be determined from a surface or volumetric heating source equation [30, 31]:

$$T_\mathrm{s}(t) = \begin{cases} T_\infty + \frac{2(1-R)I_0}{k_T}\left(\frac{D_\mathrm{th}t}{\pi}\right)^{1/2} & \frac{l_T}{l_\alpha} >> 1 \\ T_\infty + \frac{\alpha_\mathrm{ext}(1-R)I_0}{\rho C_\mathrm{P}}t & \frac{l_T}{l_\alpha} << 1 \end{cases} \quad (1)$$

Table 1 Thermodynamic and optical (at λ =1064 nm) properties of silicon

Parameter	Unit	Value
Melting temperature	T_m [K]	1683 [28]
Boiling temperature	T_b [K]	2628 [28]
Vaporisation temperature	T_v [K]	3543 [28]
Reflectivity $T < T_\mathrm{m}$	R [–]	$\frac{35.5+3.6\times10^{-3}T}{100}$ [29]
Reflectivity $T > T_\mathrm{m}$	R [–]	0.72 [29]
Absorption coefficient $T < T_\mathrm{m}$	α [cm^{-1}]	10^5 [29]
Absorption coefficient $T > T_\mathrm{m}$	α [cm^{-1}]	1.13×10^6 [29]

where T_∞ is the ambient temperature, and the ratio of the thermal and optical penetration depths is $l_T/l_\alpha \simeq 2\alpha_\mathrm{ext}\sqrt{D_\mathrm{th}\tau_L}$. In the case of a pulse with a Gaussian spatial profile the relations above are not necessarily satisfied across the spatial profile. Further, the depth to which melting will occur depends on the specific conditions under which energy is deposited into the material. Thermal penetration depth l_T is often a reasonable estimate for melt depth but under energetic ablation conditions cannot adequately describe the melt depth due to the complex dynamics of the process.

For surface heating in the case of semi-transparent materials, the peak power P_peak is required to exceed a threshold value (tantamount to a temperature increase) in which case the surface of the target can be changed into a conducting state, leading to an increase in the absorption coefficient α_ext that is typically higher than the solid state value. In the case where P_peak does not exceed the critical value, the remainder of the pulse will penetrate to the full optical penetration depth leading to volume heating and defines the initial geometry of the source term prior to the onset of any thermo-mechanical response by the material.

In the case of "long" pulse durations where the pulse duration τ_L, electron cooling time τ_e and lattice heating time τ_i satisfy the condition $\tau_\mathrm{e} << \tau_\mathrm{i} << \tau_\mathrm{L}$ thermal equilibrium between the electrons and lattice can be assumed [32]. Electron-lattice coupling occurs on a much shorter timescale than the pulse duration leading to the macroscopic treatment of the temperature; electron and lattice temperatures can be assumed to, therefore, satisfy $T = T_\mathrm{e} = T_\mathrm{i}$. Electron and lattice heat capacities, thermal diffusivity and other thermal, optical and mechanical properties can be treated as the bulk values specific to the material, shown in Table 1 for silicon. Thermal diffusion into a material is characterised by the thermal conductivity, bulk heat capacity and pulse duration, and can be approximated by [28, 32]:

$$l_T \simeq 2\left(\frac{k_T\tau_\mathrm{L}}{\rho C_\mathrm{p}}\right)^{1/2} \quad (2)$$

, where the thermal diffusivity is defined as:

$$D_\mathrm{th} = \frac{k_\mathrm{T}}{\rho C_\mathrm{p}}, \quad (3)$$

and k_T is the thermal conductivity and C_p is the bulk heat capacity. The models above are caveated by temporal constraints that determine the thermodynamic regime conditions. The loss of long-range order in the atomic lattice leads to changes in the bulk thermal and optical properties of the material. Changes in heat capacity, thermal diffusion,

thermal conductivity, absorptivity and reflectivity are phenomenological consequences of a temperature rise that have a critical influence on the specific energy distribution at the interaction zone, and determine the nature and timescale of the material removal mechanism. In the case of silicon it takes about an eighth of the energy to remove the same mass of material by melting as opposed to vaporisation. In the nanosecond regime, thermal and structural effects dominate with melt expulsion being the dominant material removal mechanism, at moderate fluence levels [20]. Recoil pressure resulting from the emission of a shockwave as well as backward travelling shockwaves have been attributed to material ejection when it interacts with an interface separating two different fluids, known as the the Richtmyer–Meshkov instability [33]. Molten material is often observed long after pulse termination, demonstrated in the case of nanosecond pulses [30, 31] and involves the interplay of several phenomena including hydrodynamic instabilities and vapour-assisted ejection. Surface vapour pressure as well as supra-surface ejecta detonations have also been attributed to melt ejection via pressure gradients across the irradiated zone [13, 34]. The specific mechanisms responsible for material ejection depend on the geometry and rate of energy deposition.

3 Materials and experimental procedure

The laser system used is a Yb-doped, all-fibre MOPA [35], operating at $\lambda = 1060$ nm, capable of generating various custom-defined temporal pulse shapes. A pulse shape is programmed into the seed diodes, amplified and delivered to the sample in a pulse train. The scanner (Cambridge Technology Lightning II) speed (4.5 ms^{-1}) and laser pulse repetition rate (60 kHz) were adjusted so as to separate the individual laser spots (separation of 75 µm). This way it is possible to examine the effects of a variety of single-pulse profiles on the long-range morphology. A sample is placed on a moveable lab-jack and the position relative to the scan lens focal length (160 mm) is measured using a dial gauge. For all trials, optical parameters were kept constant, producing a minimum D_{86} spot size (the value at which the intensity value drops to $1/e^2$ of the maximum) of 35 µm. All processing trials were carried with the focal plane at the sample surface.

The experiments in this work were carried out on monocrystalline silicon wafer sections, 650 µm thick, with a $< 1|1|1 >$ crystallographic orientation. The silicon wafer was laser sectioned into 5×15 mm samples for processing. The surface of the silicon was considered to be of optical quality and no further pre-processing was carried out. During processing, no gas assistance was used and all tests were carried out at an ambient conditions. No post-processing (such as ultrasonic cleaning) was carried out, precisely because this would create ambiguity with respect to pulse profile effects on surface morphology.

A range of pulse envelopes with a high front peak followed by a decaying tail (FPDT) pulse envelopes (see Fig. 1) is tested to determine the relative contribution of peak power, pulse duration and overall pulse energy on the material response. The first two parameters are kept constant while the energy of the pulse is varied. This is accomplished by depleting the energy from the pulse tail or by packing additional energy into it: the two energy regimes are named FPDT-D (fast decay rate) and FPDT-E (slow decay rate), for depleted and energised pulses, respectively. Figure 1 shows the two pulse regimes with energised and depleted pulses. The front peak power and pulse duration are varied independently. Peak powers of $P_{peak} = 1, 2, 4, 6, 8$ and 10 kW were tested for pulse durations of $\tau_L = 50, 60, 70, 100$ and 150 ns for FPDT-E and FPDT-D pulses. FPDT-D pulses reach peak power in 6–7 ns while FPDT-E pulses reach peak power in 16–19 ns.

4 Results

4.1 Material transport mechanisms

Because of cumulative heating effects it is difficult to categorically state the dominant mechanism during crater formation. It is, however, possible to gain insight into the material transport mechanisms. In this study, six distinct regimes can be differentiated, presented in order of increasing energetic cost:

- Melt displacement characterised by large molten lips at the crater edge and smooth molten clumps near the crater, as shown in Fig. 2a. Energy is absorbed volumetrically, heating the material to a depth defined by the optical penetration depth, increasing the temperature to T_m. The molten material is displaced by surface tension away from the crater centre towards the cooler edge forming the lip crater. Hydrodynamic instabilities lead to mechanical fluctuations in the liquid separating small droplets which are deposited close to the crater.
- Melt ejection limited molten lip and clumping with molten streaks extending radially away from the crater centre, as shown in Fig. 2b. Energy is absorbed volumetrically, melting the material and creating a high-pressure region at the centre of the crater. Clumps of molten material are ejected away from the centre forming the characteristic molten streaks before solidifying on the surface.
- Layered melting characteristics of both melt displacement and melt ejection mechanisms. Additionally, it is characterised by visible ripples along the crater surface,

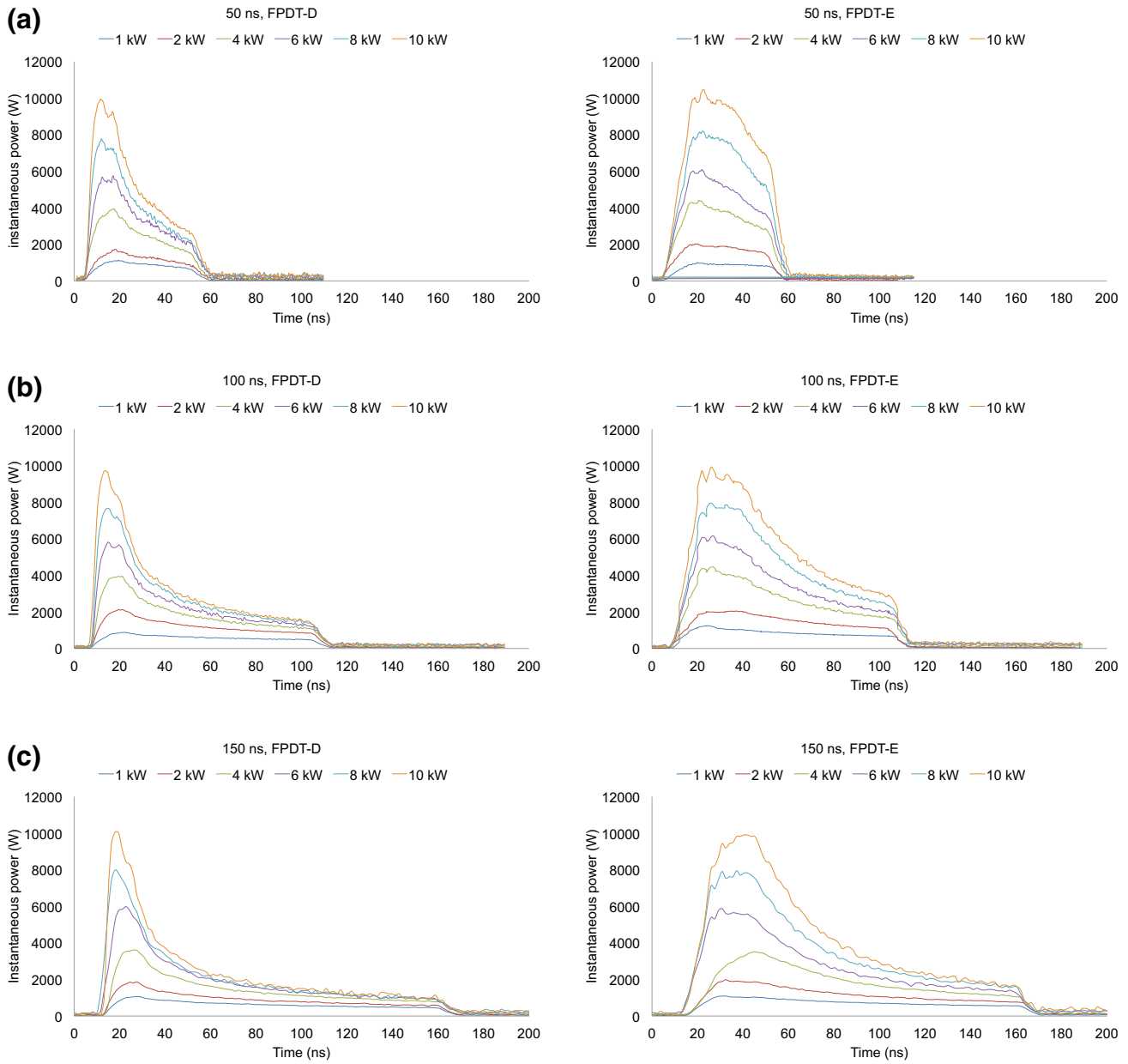

Fig. 1 Examples of **a** 50 ns, **b** 100 ns and **c** 150 ns FPDT-D and FPDT-E pulses. In all cases, the same peak power and pulse duration are achieved, except that FPDT-E achieves peak power in ≃ 16–19 ns while FPDT-D reaches peak power in ≃ 6–7 ns

as shown in Fig. 2c. Layered melting is a transitional mechanism between melt ejection and vaporisation.

– Vaporisation characterised by a reduction of melt pools and an increase in micrometre-sized particles. Additionally, a thin layer of re-condensed dust is evident, as shown in Fig. 2d. The material is surface heated due to energy confinement effects with vaporisation of a thin surface layer. The surface layer recedes immediately behind the vaporisation front. Melt ejection is limited as a result.
– Nucleated vaporisation characterised by bubble craters at the bottom of the main crater and thin extended streaks away from the crater. Additionally, large clumps surround the crater edge, as shown in Fig. 2e. Energy is absorbed volumetrically with nucleation centres forming in the molten volume. The explosive nature of the ejection means that molten clumps appear.
– Limited plasma formation—presence of both small rough clumps and particulates around the crater are characteristic of vapour re-condensation, as well as nucleated craters

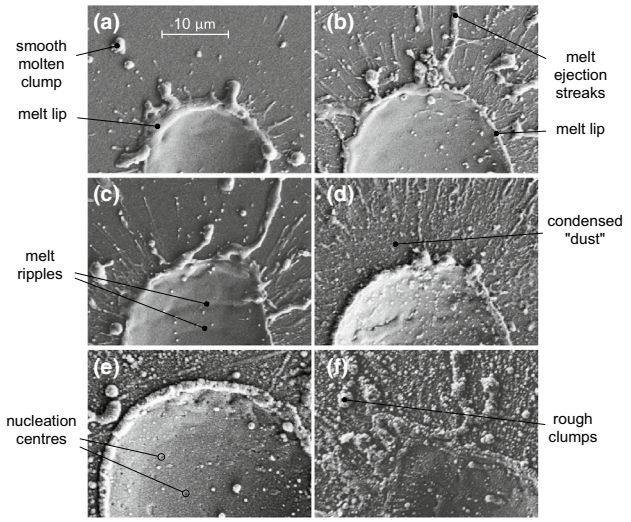

Fig. 2 Examples of material transport mechanisms evident under studied conditions **a** melt displacement, **b** melt ejection, **c** layered melting, **d** vaporisation, **e** nucleated vaporisation and **f** limited plasma formation

at the bottom of the main crater, as shown in Fig. 2f. Ejected vapour is heated by the remainder of the pulse igniting a plasma. Re-condensed material coats the surface with re-condensed sub-micrometre particles.

4.2 Energy transport dependence on temporal envelope

Figure 3 shows SEM images of the crater morphology for (a) energy depleted pulses and (b) energised pulses. The dashed lines represent the approximate boundaries when different mechanisms become evident. Although the different regions are represented as discrete transitions, in reality the contribution of each mechanism will vary gradually with pulse parameters. Additionally, this implies that any one of the described mechanisms does not necessarily occur across the entire site. The degree of contribution to the long-range morphology of the crater is complicated by the Gaussian intensity distribution in the spatial domain. Finally, the time taken to reach pulse peak power (and its final value) sets the initial conditions while the tail of the pulse determines the type, and evolution, of material transport mechanisms.

Melt displacement is typically confined to low peak power and short pulse durations. Layered melting transitions to nucleated vaporisation increases with both peak power and pulse duration while the transition to vaporisation is predominantly a peak power phenomena. Vaporisation conditions can also be reached by a direct transition from melt expulsion by adding additional energy in the pulse tail (controlled by varying the pulse duration). Nucleated vaporisation can occur through layered melting if the molten surface does not recede sufficiently quickly—so as to be ejected away from the centre—and is thus raised to vaporisation temperature volumetrically, seeding nucleation in the superheated volume. Similarly, a direct transition from vaporisation to nucleated vaporisation can occur if the rate of surface vaporisation is exceeded by volumetric etching rate. Plasma formation can only occur if a vapour plume is already present and the pulse has not yet terminated. The residual energy in the pulse tail further energises the vapour plume and can ignite a plasma. No direct transitions to the plasma phase are possible and an initial phase transition to the vapour phase is prerequisite for plasma formation.

Notably, almost all regimes can be reached by manipulating the peak power or pulse duration independently. The exception is the special case of layered melting, which requires that enough energy is delivered at any point in time to keep the material in a molten state, while at the same time allowing time for the molten material to displace within the time frame of the pulse (τ_L).

4.2.1 Energy packing consequence on crater geometry

Packing extra energy into the tail of the pulse acts primarily to shift the material response regime and has relatively little influence on the penetration depth or penetration efficiency. Figure 4a shows the penetration depth data for the two pulse types. The solid and dashed lines represent the theoretical thermal penetration limit given a diffusion time τ_L. As silicon temperature rises to melting temperature T_m, the thermal conductivity drops rapidly by an order of magnitude of its $T = 293$ K level, while the heat capacity increases by a factor of 1.4 over the same range.

Initially, the material is assumed to be volumetrically heated; the entire volume will experience a temperature rise and will experience a change in C_p and k_T. If the assumption is made that the material is heated to the melting temperature quickly (evidenced by the analysis presented in previous section), the thermal diffusion length will be defined by the thermal conductivity and heat capacity at $T = T_m$. The time taken to reach the melting temperature is primarily set by the intensity of the leading edge of the pulse, i.e. the rate of energy deposition.

The extra energy in the tail is used primarily to shift the material response regime from low-energy regimes to vaporisation and plasma formation. The increase in energy represents an increase in initial peak power along each data set and an increase in tail energy between data sets. Clearly there is no crater depth advantage to be gained by packing additional energy to the tail of the pulse, while diameter increases are minimal and only apparent at long pulse durations for the two pulse types. The crater depths are calculated using Eq. (2). It has to be noted that the relationship Eq. (2)

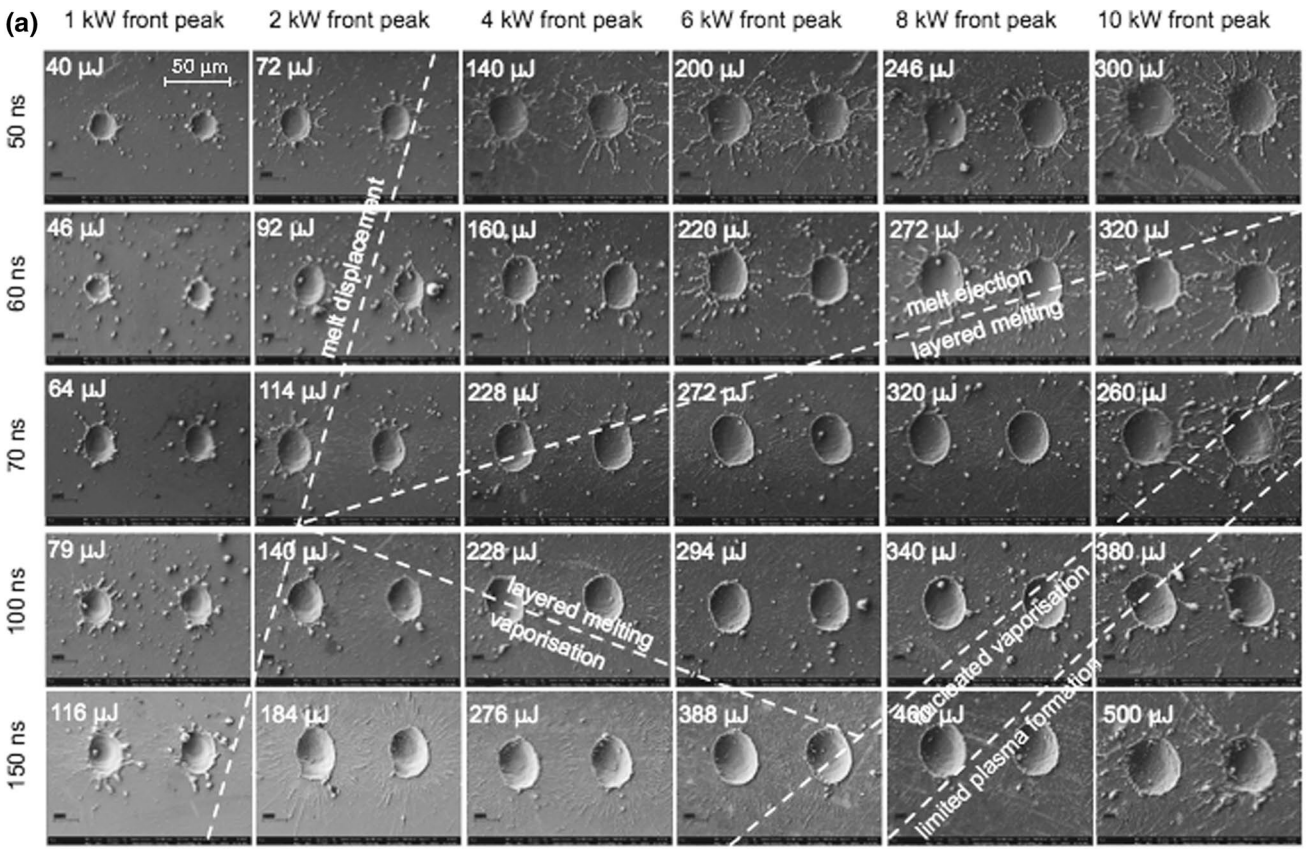
(a)
1 kW front peak
2 kW front peak
4 kW front peak
6 kW front peak
8 kW front peak
10 kW front peak
50 ns
60 ns
70 ns
100 ns
150 ns
40 µJ
50 µm
72 µJ
140 µJ
200 µJ
246 µJ
300 µJ
46 µJ
92 µJ
160 µJ
220 µJ
272 µJ
320 µJ
melt displacement
melt ejection
layered melting
64 µJ
114 µJ
228 µJ
272 µJ
320 µJ
260 µJ
79 µJ
140 µJ
228 µJ
294 µJ
340 µJ
380 µJ
layered melting
vaporisation
nucleated vaporisation
116 µJ
184 µJ
276 µJ
388 µJ
460 µJ
500 µJ
limited plasma formation

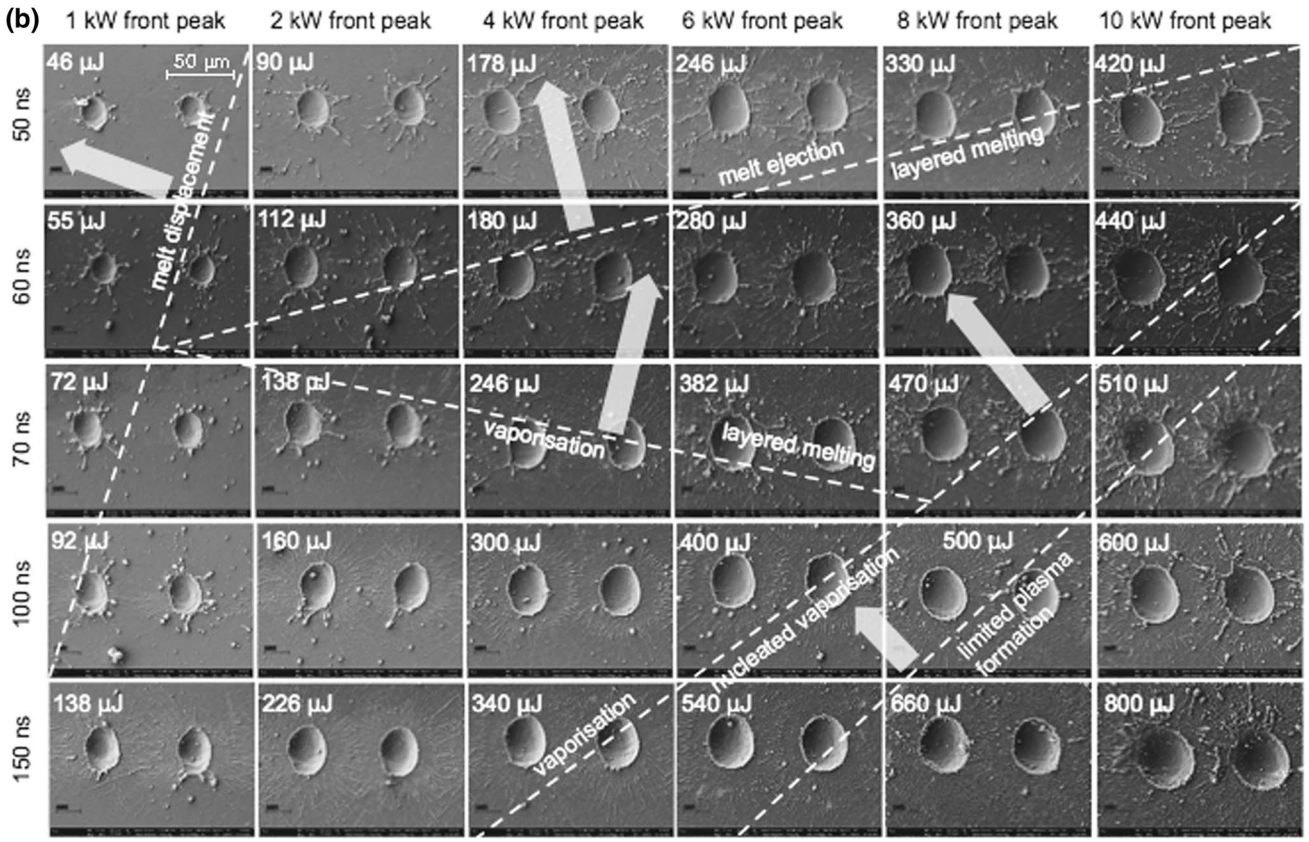
(b)
1 kW front peak
2 kW front peak
4 kW front peak
6 kW front peak
8 kW front peak
10 kW front peak
50 ns
60 ns
70 ns
100 ns
150 ns
46 µJ
50 µm
90 µJ
178 µJ
246 µJ
330 µJ
420 µJ
melt displacement
melt ejection
layered melting
55 µJ
112 µJ
180 µJ
280 µJ
360 µJ
440 µJ
72 µJ
138 µJ
246 µJ
382 µJ
470 µJ
510 µJ
vaporisation
layered melting
92 µJ
160 µJ
300 µJ
400 µJ
500 µJ
600 µJ
nucleated vaporisation
limited plasma formation
138 µJ
226 µJ
340 µJ
540 µJ
660 µJ
800 µJ
vaporisation

◂**Fig. 3** SEM images of single-pulse interactions for $P_{peak} = 1, 2, 4, 6, 8$ and 10 kW and pulse durations of $\tau_L = 50, 60, 70, 100$ and 150 ns for **a** FPDT-D and **b** FPDT-E pulses. The white arrows indicate the material response regimes shift

is primarily valid for an initially confined source term that thermalises the surrounding material during its existence; it does not take into account the original geometry of the heating source. For metals, the optical penetration is on the order of nanometers, confining the source term to a thin disc at the sample surface. When machining silicon using $\lambda = 1060$ nm, however, the initial source geometry will evolve as a cylindrical volume, with hemispherical energy distribution rather than a surface disc geometry owing to the higher optical penetration depth. As such, the heating source propagates deeper within the material.

Crater aspect ratio (the ratio of crater width to crater depth) remains relatively constant for $\tau_L > 50$ ns over a range of energies. For $\tau_L < 100$ ns the relative energy contribution to the edges of the crater decreases leading to an increase in crater depth while leaving the diameter relatively unaffected.

4.2.2 Energy packing consequence on penetration efficiency

Penetration efficiency (defined as the ratio of crater depth to pulse energy) lines are presented in Figure 5. Penetration

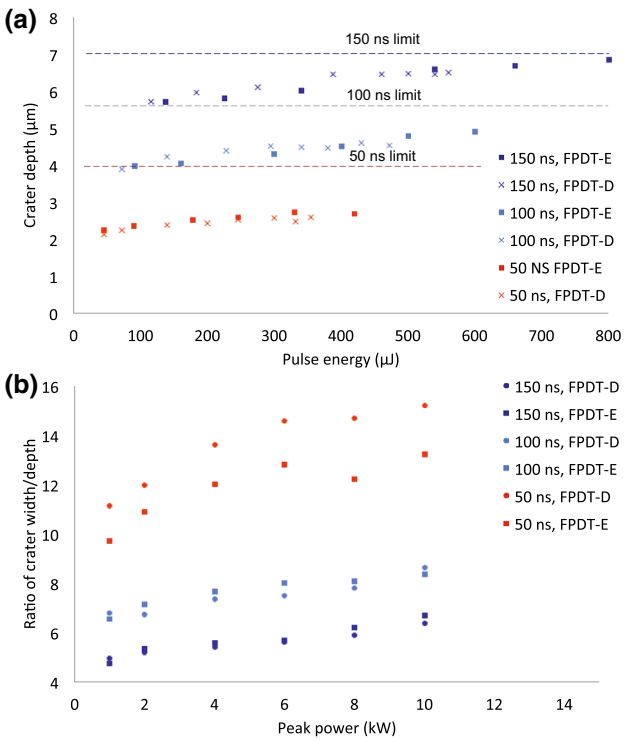

Fig. 4 **a** The measured and theoretical penetration depth data for the two pulse types and **b** the ratio of crater width to depth

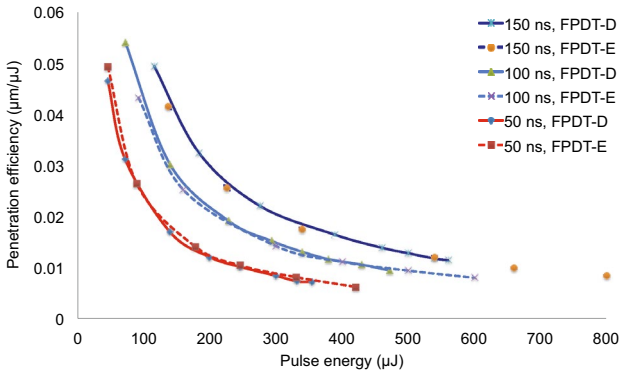

Fig. 5 Penetration efficiency data for the two pulse types showing that penetration efficiency is energy limited for a given pulse duration

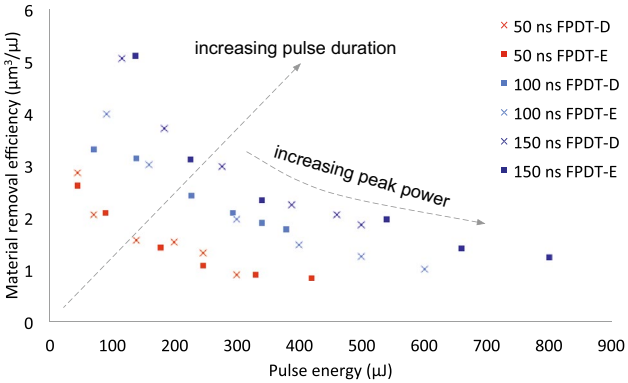

Fig. 6 Material removal efficiency for FPDT-E and FPDT-D pulses from single-pulse interactions. The arrows show inclusion of additional energy either through pulse duration extension or through increasing peak power

efficiency saturates at each pulse duration: a limit of penetration efficiency exists that is set by the pulse duration, and cannot be exceeded by adding additional energy to the pulse, and is a duration limiting process for a given pulse duration.

4.2.3 Energy packing consequence on material removal efficiency

Figure 6 shows material removal efficiency, defined as the crater volume per unit energy. Similar to penetration depth, longer pulses achieve superior material removal efficiency. Further, the increase in total material removed when additional energy is packed to the pulse is negligible and can be explained by noting that additional energy is progressively used up to move the interaction to energetically costlier regimes, and widening the crater diameter through lateral thermal diffusion.

5 Conclusions

A range of pulse envelopes have been tested on < 1|1|1 > mono-crystalline silicon. Six regimes of material ejection were identified and disambiguated with respect to energy packing considerations over a range of pulse envelopes. The effects of energy packing have been shown for long pulse interactions to have a relatively small impact on penetration depth or material removal rate efficiency. Penetration efficiency analysis shows that there is a limit that is primarily set by the pulse duration, while the exact efficiency depends on the specific temporal form. A melt-dominated regime has universally been shown to have the best penetration efficiency but leads to significant processing artefacts, occurring through either thermal incubation for long pulses or forced through source term control on the basis of the state of the material.

Contributions from dynamic aspects of the interaction clearly play an important part in the saturation effect of both the machined depth and material removal efficiency. This effect has previously been demonstrated to have a profound impact on the post-process morphology of the site through plume and plasma-enhanced surface heating [6, 36]. Onset of these phenomena leads to secondary energy coupling with molten ejecta, vapour or plasma that can have a profound effect on the dynamics of the interaction and the final morphology of the affected site. Alternatively, the energy contained in the tail can also be reflected (lost) at the shock-wave interface where there is a significant refractive index difference between the leading edge of the shock and the surrounding gas, air in our case.

Energy packing has been shown to shift the interaction to energetically costlier regimes without appreciable benefit in depth, material removal or crater morphology and quality. We conclude by remarking that based on this work, it should be possible to further tailor the temporal energy envelope to create highly energy-efficient ablative events, by taking advantage of the temporal pulse asymmetry and matching this to the required material response.

Acknowledgements The authors would like to thank the UK Technology Strategy Board under project TP14/HVM/6/I/BD5665. The authors acknowledge the EPSRC Centre for Doctoral Training in Photonic Systems Development for their generous support.

References

1. H. Schittenhelm, G. Callies, P. Berger, H. Hugel, Measurements of wavelength-dependent transmission in excimer laser-induced plasma plumes and their interpretation. J. Phys. D Appl. Phys. **31**(418), 418–427 (1998)
2. J.-F.Y. Gravel, D. Boudreau, Study by focused shadowgraphy of the effect of laser irradiance on laser-induced plasma formation and ablation rate in various gases. Spectrochim. Acta Part B At. Spectrosc. **64**(1), 56–66 (2009)
3. D. Breitling, H. Schittenhelm, P. Berger, F. Dausinger, H. Hügel, Shadowgraphic and interferometric investigations on Nd: YAG laser-induced vapor/plasma plumes for different processing wavelengths. Appl. Phys. A Mater. Sci. Process. **69**(7), S505–S508 (1999)
4. A.V. Bulgakov, N.M. Bulgakova, Dynamics of laser-induced plume expansion into an ambient gas during film deposition. Phys. D Appl. Phys. **28**(8), 1710–1718 (1995)
5. A. Bogaerts, Z. Chen, Effect of laser parameters on laser ablation and laser-induced plasma formation: a numerical modeling investigation. Spectrochim. Acta Part B At. Spectrosc. **60**(9–10), 1280–1307 (2005)
6. K. Pangovski, M. Sparkes, W. O'Neill, A holographic method for optimisation of laser-based production processes. Adv. Opt. Technol. **5**(2), 177–186 (2016)
7. Lu Quanming, S.S. Mao, X. Mao, R.E. Russo, Delayed phase explosion during high-power nanosecond laser ablation of silicon. Appl. Phys. Lett. **80**(17), 3072 (2002)
8. Y. Zhou, W. Benxin, S. Tao, A. Forsman, Yibo Gao, Physical mechanism of silicon ablation with long nanosecond laser pulses at 1064 nm through time-resolved observation. Appl. Surf. Sci. **257**(7), 2886–2890 (2011)
9. S. Tao, Y. Zhou, W. Benxin, Y. Gao, Infrared long nanosecond laser pulse ablation of silicon: Integrated two-dimensional modeling and time-resolved experimental study. Appl. Surf. Sci. **258**(19), 7766–7773 (2012)
10. J.H. Yoo, S.H. Jeong, X.L. Mao, R. Greif, R.E. Russo, Evidence for phase-explosion and generation of large particles during high power nanosecond laser ablation of silicon. Appl. Phys. Lett. **76**(6), 783 (2000)
11. J. Lopez, A. Lidolff, M. Delaigue, C. Hönninger, E. Mottay, Comparison of picosecond and femtosecond laser ablation for surface engraving of metals and semiconductor. In: 12th International Symposium on Laser Precision Microfabrication vol. 8243, pp. 1–5 (2011)
12. B. Rethfeld, A. Kaiser, M. Vicanek, G. Simon, Ultrafast dynamics of nonequilibrium electrons in metals under femtosecond laser irradiation. Phys. Rev. B **65**(21), 214303 (2002)
13. A .C. Forsman, P .S. Banks, M .D. Perry, E .M. Campbell, A .L. Dodell, M .S. Armas, Double-pulse machining as a technique for the enhancement of material removal rates in laser machining of metals. J. Appl. Phys. **98**(3), 033302 (2005)
14. X.D. Wang, A. Michalowski, D. Walter, S. Sommer, M. Kraus, J.S. Liu, F. Dausinger, Laser drilling of stainless steel with nanosecond double-pulse. Opt. Laser Technol. **41**(2), 148–153 (2009)
15. J.S. Liu, F. Dausinger, D. Walter, M. Kraus, A. Michalowski, S. Sommer, X.D. Wang, Laser drilling of stainless steel with nanosecond double-pulse. Opt. Laser Technol. **41**, 148–153 (2009)
16. V.P. Veiko, V.N. Lednev, S.M. Pershin, A.A. Samokhvalov, E.B. Yakovlev, IYu. Zhitenev, A.N. Kliushin, Double nanosecond pulses generation in ytterbium fiber laser. Rev. Sci. Instrum. **87**(6), 063114 (2016)

17. C.M. Liebig, P. Srisungsitthisunti, A.M. Weiner, X. Xu, Enhanced machining of steel using femtosecond pulse pairs. Appl. Phys. A **101**(3), 487–490 (2010)
18. Q. Li, Y. Zheng, Z. Wang, T. Zuo, A novel high-peak power double AO Q-switches pulse Nd: YAG laser for drilling. Opt. Laser Technol. **37**(5), 357–362 (2005)
19. S.T. Hendow, R. Romero, S.A. Shakir, P.T. Guerreiro, Percussion drilling of metals using bursts of nanosecond pulses. Opt. Express **19**(11), 10221–31 (2011)
20. W. O'Neill, K. Li, High-quality micromachining of silicon at 1064 nm using a high-brightness MOPA-based 20-W Yb fiber laser. IEEE J. Sel. Top. Quantum Electron. **15**(2), 462–470 (2009)
21. P. Deladurantaye, D. Gay, A. Cournoyer, V. Roy, B. Labranche, M. Levesque, Y. Taillon. Material micromachining using a pulsed fiber laser platform with fine temporal nanosecond pulse shaping capability. In: Denis V. Gapontsev, Dahv A. Kliner, Jay W. Dawson, and Kanishka Tankala, editors. SPIE Fiber Lasers VI: Technology, Systems, and Applications, vol. 7195, pp. 71951S–71951S–12. SPIE, (2009)
22. K. Li, W. O'Neill, Fibre laser microvia drilling and ablation of Si with tuneable pulse shapes. Int. J. Precis. Eng. Manuf. **13**(5), 641–648 (2012)
23. Hans Herfurth, Rahul Patwa, Tim Lauterborn, Stefan Heinemann, Henrikki Pantsar, Micromachining with tailored nanosecond pulses. Photonics North 2007 **6796**, 67961G–67961GÃ¢â‚¬â„¢8 (2007)
24. K.A. Mumtaz, N. Hopkinson, Selective laser melting of thin wall parts using pulse shaping. J. Mater. Process. Technol. **210**(2), 279–287 (2010)
25. S.T. Hendow, S.A. Shakir, Structuring materials with nanosecond laser pulses. Opt. Express **18**(10), 10188–99 (2010)
26. T.C. Gunaratne, X. Zhu, V.V. Lozovoy, M. Dantus, Influence of the temporal shape of femtosecond pulses on silicon micromachining. J. Appl. Phys. **106**(12), 1–5 (2009)
27. K. Pangovski, M. Sparkes, A. Cockburn, W. O'Neill, D. Richardson, Control of material transport through pulse shape manipulation a development toward designer pulses. IEEE J. Sel. Top. Quantum Electron. **20**(5), 51–63 (2014)
28. R. Poprawe, H. Weber, G. Herziger (eds.), *Laser Physics and Applications Subvolume C : Laser Applications*, vol. 1 (Springer, 2004)
29. J.H. Yoo, S.H. Jeong, R. Greif, R.E. Russo, Explosive change in crater properties during high power nanosecond laser ablation of silicon. J. Appl. Phys. **88**(3), 1638 (2000)
30. G.E.Jr Jellison, Measurements of the optical properties of liquid silicon and germanium using nanosecond timeresolved ellipsometry. Appl. Phys. Lett. **51**(5), 352–354 (1987)
31. G.E. Jellison Jr., D.H. Lowndes, D.N. Mashburn, R.F. Wood, Time-resolved reflectivity measurements on silicon and germanium using a pulsed excimer KrF laser heating beam. Phys. Rev. B **34**(4), 2407 (1986)
32. B.N. Chichkov, C. Momma, S. Nolte, F. von Alvensleben, a Tünnermann, Femtosecond, picosecond and nanosecond laser ablation of solids. Appl. Phys. A Mater. Sci. Process. **63**(2), 109–115 (1996)
33. S.-B. Wen, X. Mao, R. Greif, R.E. Russo, Laser ablation induced vapor plume expansion into a background gas. II. Experimental analysis. J. Appl. Phys. **101**(2), 023115 (2007)
34. M. Schneider, Study of hole properties in percussion regime with a new analysis method. J. Laser Micro/Nanoeng. **2**(2), 128–132 (2007)
35. A. Malinowski, K.T. Vu, K.K. Chen, J. Nilsson, Y. Jeong, S. Alam, D. Lin, D.J. Richardson., High power pulsed fiber MOPA system incorporating electro-optic modulator based adaptive pulse shaping. Opt. Express **17**(23), 20927–37 (2009)
36. S.S. Mao, X. Mao, R. Greif, R.E. Russo, Influence of preformed shock wave on the development of picosecond laser ablation plasma. J. Appl. Phys. **89**(7), 4096 (2001)